

Quantifying and Bridging the Fidelity Gap: A Decisive-Feature Approach to Comparing Synthetic and Real Imagery

Danial Safaei*, Siddhartha Khastgir*, Mohsen Alirezai†, Jeroen Ploeg†, Son Tong† and Xingyu Zhao*

*WMG, University of Warwick, Coventry, U.K.

†Siemens Digital Industries Software

Abstract—Virtual testing using synthetic data has become a cornerstone of autonomous vehicle (AV) safety assurance. Despite progress in improving visual realism through advanced simulators and generative AI, recent studies reveal that pixel-level fidelity alone does not ensure reliable transfer from simulation to the real world. What truly matters is whether the system-under-test (SUT) bases its decisions on the same causal evidence in both real and simulated environments—not just whether images “look real” to humans.

This paper addresses the lack of such a behavior-grounded fidelity measure by introducing Decisive Feature Fidelity (DFF), a new SUT-specific metric that extends the existing fidelity spectrum to capture *mechanism parity*—the agreement in causal evidence underlying the SUT’s decisions across domains.

DFF leverages explainable-AI (XAI) methods to identify and compare the decisive features driving the SUT’s outputs for matched real-synthetic pairs. We further propose practical estimators based on counterfactual explanations, along with a DFF-guided calibration scheme to enhance simulator fidelity.

Experiments on 2126 matched KITTI-VirtualKITTI2 pairs demonstrate that DFF reveals discrepancies overlooked by conventional output-value fidelity. Furthermore, results show that DFF-guided calibration improves decisive-feature and input-level fidelity without sacrificing output value fidelity across diverse SUTs.

I. INTRODUCTION

Scenario-based virtual testing with synthetic data is a standard for AV safety evaluation [1], [2], enabling the recreation of complex driving situations.

Substantial resources are being directed toward the development of high-fidelity simulators [3] and generative-AI techniques [4], [5] to enhance realism to better reflect actual driving conditions. Most existing efforts have concentrated on improving “pixel-level realism”, that is, aligning synthetic *image* data with real image data in a way that is agnostic to the system-under-test (SUT). For brevity we focus on image-based data and refer to pixels when discussing input-level fidelity, but the proposed approach extends to other modalities such as LiDAR by replacing pixel correspondence with point-cloud correspondence.

However, recent studies suggest that pixel-level, SUT-agnostic fidelity does not assure reliable transfer of AV assessment conclusions between the virtual and real domains. What truly matters is whether the AV grounds its behaviors or decisions on the same underlying principles in both real and synthetic domains [6]–[9]. This emerging consensus has

shifted attention from pixel-level realism of the data towards behavioral consistency of the SUT as a more meaningful indicator of simulation validity [10]–[13].

The top part of Fig. 1 recalls the input/latent/output/safety-aware fidelity spectrum of [6]. The bottom part illustrates our extension: an XAI explainer extracts decisive features from the SUT for each paired real and synthetic input, the distance between decisive maps yields a DFF estimate, and this estimate is fed back to a calibrator that adjusts generator knobs to close mechanism gaps. The previous work [6] systematically categorized synthetic-data fidelity into four levels, as shown in Fig. 1:

input-level (IV) fidelity, latent-feature (LF) fidelity, output-value (OV) fidelity, and safety-aware (SA) fidelity. As the names suggest, these correspond respectively to the fidelity measured in the SUT’s input space (e.g., the perception neural network’s raw inputs), latent feature space, output vector space, and safety-critical output space. While this spectrum of fidelity spans the entire processing pipeline of a neural network, it remains too coarse to capture *why* the SUT exhibits the same or different behaviors when presented with paired real and synthetic inputs representing the same scenario. For example, an AV perception module may output the same steering command, say a 20-degree left turn, for both the real and synthetic inputs, implying high OV-fidelity. Yet *the underlying reasons could differ*: the real image might trigger the action due to a detected dog ahead, whereas in the synthetic version of the same scenario, the same decision arises from detecting a right-turn sign next to the dog (and the dog is misdetected, which is concerning). In this case, the system produces the same decision for different reasons, i.e., based on different causal evidence. Notably, the LF-fidelity defined in [6] cannot fully capture such discrepancies, as it simply compares all extracted features without distinguishing those that actually influence the SUT’s decision. This reveals a gap: existing metrics tell us *what* the SUT outputs, but not *why*. We need a metric that checks whether the SUT uses the same visual evidence (e.g., road edges, lane markings) in both domains. This gap directly motivates DFF. Throughout this paper, we evaluate and calibrate synthetic data for *testing* a fixed SUT; we do not train or adapt the SUT itself.

To bridge this gap, we propose an explainable-AI (XAI)-based fidelity metric that *quantifies the differences in the*

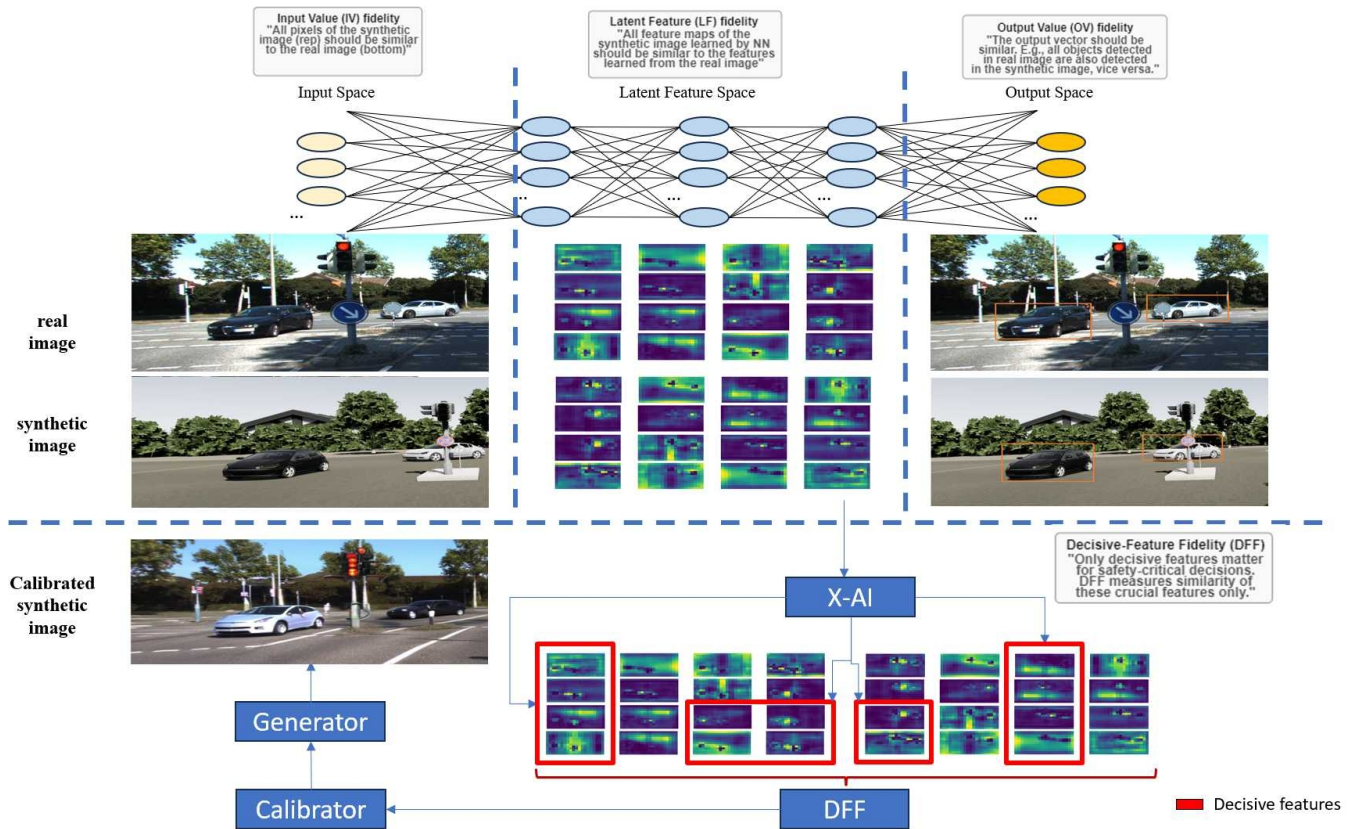


Fig. 1. Top: three levels of the fidelity spectrum (IV, LF, OV) from [6]. Bottom: our extension that adds decisive-feature fidelity (DFF) and a calibrator to adjust the generator. Safety-aware fidelity (SA) is defined in [6] but is not explicitly visualized here.

decisive features influencing the SUT's outputs for a given pair of real and synthetic data. Specifically, we first formalize a new SUT-specific fidelity metric, termed Decisive Feature Fidelity (DFF), which extends the fidelity spectrum defined in [6].

Unlike the LF-fidelity in [6], which compares all extracted features, DFF uses recent XAI methods to estimate and compare only the (subset of) features that truly influence the SUT's output.

We then design practical estimators based on counterfactual explanations to quantify DFF and use these estimates as feedback signals to *recalibrate* the synthetic data generator, thereby improving fidelity.

In our experiments we instantiate G with a diffusion-based generator, but the proposed calibration objective is general and applies equally to reconfigurable simulators such as CARLA or PreScan.

To validate our approach, we conduct experiments on 2126 matched KITTI–VirtualKITTI2 pairs across three SUTs (steering, YOLOP drivable-area, and YOLOP lane-line), demonstrating the utility of DFF for both assessment and calibration.

In summary, the main contributions include:

- **A new SUT-specific fidelity metric:** We formalize DFF, a metric that measures mechanism parity. We contrast it with existing metrics, arguing that focusing on the *decisive-feature subspace* is more meaningful than comparing raw

inputs (IV), entire latent spaces (LF), or just final outputs (OV) of the SUT.

- **An XAI-based DFF estimator:** We develop a practical estimator, using XAI methods such as counterfactual explainers (CF-XAI). The decisive maps for real and synthetic inputs are computed independently and then compared within this subspace.
- **A DFF-guided calibration objective:** We formulate an optimization objective that utilizes DFF estimates as feedback signals to fine-tune the synthetic data generator. Validation on a held-out split demonstrates that this approach improves decisive-feature and input-level fidelity. Crucially, it preserves behavioral (OV) fidelity, ensuring that the SUT's task performance does not degrade beyond a strictly defined tolerance (a pre-declared non-inferiority margin).

II. RELATED WORK

Virtual testing offers a scalable and risk-free way to assess AV safety across diverse scenarios. However, the fidelity of synthetic data used in such testing remains a critical and actively studied issue due to the persistent sim-to-real gap [3], [14]–[16]. While fidelity can be defined and classified in multiple ways, an important distinction lies between SUT-agnostic and SUT-specific measures. This perspective sets the foundation for the subsequent review of related works.

A. SUT-Agnostic Approaches to Fidelity

Domain randomization applies random perturbations (lighting, textures, object placement) during training to encourage models to ignore irrelevant variation; however, it can inadvertently remove task-critical structure that the SUT needs [17]. *Game-engine and physically-based rendering (PBR) synthesis* can generate large-scale, diverse scenes but does not guarantee that the SUT will process synthetic and real images through equivalent internal pathways [18], [19]. *Image-translation* methods such as SimGAN and CycleGAN learn mappings between synthetic and real domains to reduce visual discrepancy; yet without explicit semantic constraints, they may alter safety-relevant content (e.g., removing a pedestrian or shifting lane boundaries) [20], [21]. *Diffusion models with spatial control* (e.g., ControlNet) condition generation on semantic layouts or edge maps, improving structural fidelity to scene geometry; however, they do not verify whether the SUT’s internal reasoning transfers [4], [5]. Metric analyses further caution that popular perceptual scores (LPIPS, FID) correlate poorly with downstream task performance [22]. While valuable, all these methods are SUT-agnostic: they improve visual similarity without checking whether the SUT relies on the same causal evidence. This limitation motivates SUT-specific approaches.

B. SUT-Specific Fidelity Metrics

Recognizing the limitations of agnostic metrics, some work has moved towards SUT-specific fidelity. Studies like [23], [24] measured fidelity by comparing the SUT’s performance on real and synthetic data, which essentially corresponds to the OV-fidelity defined in [6]. Beyond OV-fidelity, [6] further introduced a spectrum of fidelity metrics spanning the input, hidden, and output layers of the SUT, assuming a neural network architecture. Moreover, it formalizes instance-level safety-aware fidelity (SA) and shows that calibrating generators to safety outcomes (i.e., those outputs that have actual safety effects on the whole AV system) aligns better with the purpose of AV testing. However, none of these metrics capture *mechanism parity*—whether the SUT made its decision for the same underlying reasons, not just whether it produced the same final output. This gap motivates the need for a decisive-feature-level metric.

Existing Fidelity Metric Blind Spots: As summarized in Table I, these established metrics have known blind spots. *IV fidelity* fails when the SUT is locally unrobust: small input perturbations invisible to pixel metrics can cause large output changes [6], [25], so high IV-fidelity does not guarantee high OV-fidelity. *OV fidelity* can mask mechanism shifts: the SUT may produce identical outputs from different causal evidence (spurious correlation). *LF fidelity*, which compares broad internal activations, conflates decisive and non-decisive features [26]; a synthetic image may activate similar neurons overall yet rely on entirely different evidence for the final decision. These gaps motivate a metric that specifically targets the *decisive* feature subspace—the subset of features that actually influence the SUT’s output.

TABLE I
FIDELITY METRICS, WHAT THEY COMPARE, AND TYPICAL BLIND SPOTS.

Notion	Comparison Target	SUT-Specific?	Blind spot
IV	pixels/appearance	No	unrobust F
OV	task outputs	Yes	spurious evidence
LF	broad internals	Yes	non-decisive channels
DFF	decisive features	Yes	unrobust XAI (mitigated)

III. FOUNDATION

We denote the SUT by a function $F : \mathbb{R}^{d_0} \rightarrow \mathbb{R}^{d_L}$ mapping d_0 -dimensional inputs to d_L -dimensional outputs, and the XAI explainer by H . We let x_r and x_s denote real and synthetic inputs, respectively. D represents the distance metric used to quantify the difference between explanations. Decisive features are evaluated through the maps $H(F(\cdot))$ and compared using D . (All notations are summarized in Appendix A.)

A. Scenario Description and Generator

Let \mathbb{A} denote the universe of semantic attributes (e.g., actors and environment factors). A scenario description is $SD = \{(a_k, v_k)\}_{k=1}^K$ with $a_k \in \mathbb{A}$ and values v_k (discrete or continuous, encoded in \mathbb{R} as needed). A synthetic generator G_Θ takes SD and produces a sample $x_s = G_\Theta(SD) \in \mathbb{R}^{d_0}$; G_Θ may be stochastic. Let $\text{RW}(SD)$ denote the (ideal) set of real samples consistent with SD . In practice one only has a collected dataset X^{cr} and an empirical approximation $\widehat{\text{RW}}(SD) = X^{cr} \cap \text{RW}(SD)$.

B. Established Fidelity Metrics

We introduce the formal definitions of fidelity metrics from [6] that are related to our DFF in this subsection. Let D_{in} be a distance on \mathbb{R}^{d_0} , D_{out} a distance on \mathbb{R}^{d_L} , and let $\varepsilon_{\text{in}}, \varepsilon_{\text{out}} > 0$.

Input-Value (IV) Fidelity: A synthetic $x_s \sim G_\Theta(SD)$ is $\langle D_{\text{in}}, \varepsilon_{\text{in}} \rangle$ -IV-fidelitous if

$$\exists x_r \in \text{RW}(SD) : D_{\text{in}}(x_s, x_r) \leq \varepsilon_{\text{in}}. \quad (1)$$

Since we only possess the empirical set $\widehat{\text{RW}}(SD)$, we evaluate Eq. (1) by minimizing over $\widehat{\text{RW}}(SD)$ instead of $\text{RW}(SD)$. Note that this upper-bounds the true minimum (a conservative approximation).

Output-Value (OV) Fidelity: Given F , $x_s \sim G_\Theta(SD)$ is $\langle F, D_{\text{out}}, \varepsilon_{\text{out}} \rangle$ -OV-fidelitous if

$$\exists x_r \in \text{RW}(SD) : D_{\text{out}}(F(x_s), F(x_r)) \leq \varepsilon_{\text{out}}. \quad (2)$$

Latent-Feature (LF) Fidelity: Beyond input/output matching, one can assess whether the SUT processes synthetic inputs through *similar internal mechanisms*. Given a deep neural network (DNN) F with intermediate layers indexed by ℓ , and using a distance D_{if} and tolerance ε_{if} :

$$\exists x_r \in \text{RW}(SD) : \forall \ell \in \mathcal{I}_\ell, D_{\text{if}}(F^{(\ell)}(x_s), F^{(\ell)}(x_r)) \leq \varepsilon_{\text{if}}, \quad (3)$$

where \mathcal{I}_ℓ denotes the set of selected intermediate layer indices of the DNN.

IV. PROPOSED SOLUTION: DECISIVE-FEATURE FIDELITY (DFF)

Our proposed framework, illustrated in Fig. 1, consists of three main components: (1) **Metric Definition**: We formalize DFF to quantify mechanism parity alongside IV and OV fidelity. (2) **Estimation**: An XAI explainer extracts decisive features from both real and synthetic inputs to compute the DFF metric. (3) **Calibration**: A feedback loop uses the DFF metric to optimize the generator’s parameters Θ , minimizing the mechanism gap. The following subsections detail each component.

A. DFF Metric Definition

Given a scenario description SD , a fixed SUT F , and per-SUT thresholds $(\varepsilon_{\text{in}}, \varepsilon_{\text{out}}, \varepsilon_{\text{dff}})$, we say that a synthetic sample $x_s \sim G_{\Theta}(SD)$ is *acceptable for virtual testing* if there exists at least one real $x_r \in \text{RW}(SD)$ such that:

- 1) IV and OV constraints (1)–(2) are satisfied.
- 2) The decisive-feature distance satisfies $D(\text{H}(F(x_s)), \text{H}(F(x_r))) \leq \varepsilon_{\text{dff}}$.

Note that we exclude LF fidelity (ε_{lf}) from the top-level acceptance criteria as DFF provides a more specific measure of internal mechanism alignment relevant to the task. The thresholds ε_{in} , ε_{out} , and ε_{dff} are user-defined hyperparameters. In practice, they are derived empirically from a calibration set (e.g., using the 95th percentile of distances between matched real pairs) or set based on industry safety standards (e.g., OV error < 5%). We instantiate decisive features via an XAI explainer H and compare them with a distance D . Formally, x_s is $\langle F, H, D, \varepsilon_{\text{dff}} \rangle$ -DFF-fidelitous with respect to x_r if

$$D(\text{H}(F(x_s)), \text{H}(F(x_r))) \leq \varepsilon_{\text{dff}}.$$

Over a paired set $\{(x_{r,i}, x_{s,i})\}_{i=1}^N$, we define the DFF pass-rate as

$$\text{Pass-Rate} = \frac{1}{N} \sum_{i=1}^N \mathbb{I}(D(\text{H}(F(x_{s,i})), \text{H}(F(x_{r,i}))) \leq \varepsilon_{\text{dff}}).$$

In our experimental evaluation (Table II), we specifically select ε_{dff} such that the pass-rate on a reference calibration set is 90% or 95% (denoted as ε_{90} and ε_{95}).

Relation to IV/OV/LF: IV enforces pixel proximity; OV enforces output proximity; LF enforces broad feature proximity. DFF enforces *decisive* feature alignment and can *diverge* from OV/LF when mechanism shifts occur (e.g., correct output for the wrong reason).

B. DFF Estimator

We instantiate DFF *exclusively* with a mask-and-infill counterfactual explainer¹ (CF-XAI) [30].

How CF-XAI works (intuition): Given an image x , the explainer asks: “What is the smallest change to x that would flip the SUT’s output?” It finds a sparse mask m^* indicating

¹Counterfactuals give intervention-style evidence and avoid well-known pitfalls of purely associative saliency, e.g., unrobustness/inconsistency of explanations [27]–[29]; we therefore choose CF-XAI. That said, conceptually any reliable XAI method can be applied in our DFF framework.

which pixels must be modified (via infill from a learned prior) to change the decision. The resulting *decisive map* $\text{H}(F(x))$ highlights these critical regions.

We compute $\text{H}(F(x_r))$ for the real image and $\text{H}(F(x_s))$ for the synthetic image using the same CF-XAI procedure applied independently. To ensure robustness against the stochastic nature of counterfactual generation, we define the decisive map as the expectation over K_{cf} random seeds ζ_k :

$$\text{H}(F(x)) := \frac{1}{K_{\text{cf}}} \sum_{k=1}^{K_{\text{cf}}} m^*(x; \zeta_k), \quad (4)$$

where $m^*(x; \zeta_k)$ is the optimal mask generated for input x using seed ζ_k . We use mean squared error (MSE) as D , computed on these averaged, pooled 16×16 decisive maps.

C. DFF-based Calibration Objective

We introduce a calibrator network C_{η} , parameterized by η . The goal of the calibrator is to predict optimal generator configuration parameters Θ^* based *only* on the synthetic context, ensuring the method is viable during testing when ground truth is absent. Given a dataset $D_{\text{paired}} = \{(x_{r,i}, x_{s,i}^{(\text{init})}, SD_i)\}_{i=1}^N$, the calibrator maps the initial synthetic sample and scenario description to the refined parameters: $\Theta_i^* = C_{\eta}(x_{s,i}^{(\text{init})}, SD_i)$. During the *training* of C_{η} , we utilize the paired real images $x_{r,i}$ to compute the loss and update η . We minimize a *combined* loss function that includes input reconstruction loss (IV), SUT output (OV) loss, and our DFF dissimilarity:

$$\eta^* = \arg \min_{\eta} \sum_{i=1}^N \left(\mathcal{L}_{\text{recon}}(x_{s,i}^*, x_{r,i}) + \beta \mathcal{L}_{\text{OV}}(F(x_{s,i}^*), F(x_{r,i})) + \lambda_{\text{dff}} \mathcal{L}_{\text{DFF}}(x_{s,i}^*, x_{r,i}) \right), \quad (5)$$

where $x_{s,i}^* = G_{\Theta_i^*}(SD_i)$, and $\mathcal{L}_{\text{recon}}$ and \mathcal{L}_{OV} are standard reconstruction (for example ℓ_1 /LPIPS) and task losses (for example MSE). We define $\mathcal{L}_{\text{DFF}}(x_s, x_r) := D(\text{H}(F(x_s)), \text{H}(F(x_r)))$. We treat F as fixed and non-differentiable and backpropagate gradients only through C_{η} into the generator knobs.

D. Calibration Implementation

Calibration knobs and optimizer: C_{η} predicts generator/post-processing parameters per scenario. We optimize the random seed using Evolution Strategies (ES; population size 32, $\sigma=0.1$). For continuous parameters specifically ControlNet scales, guidance scale, and mild post-operations (contrast/brightness/blur) we use Stochastic Gradient Descent (SGD) with learning rates of 5×10^{-3} and 1×10^{-3} respectively. Gradients backpropagate through the calibrator and generator knobs only. We treat F as fixed and non-differentiable. The DFF dissimilarity provides the signal for the optimization (SGD or ES) of these generator knobs.

Algorithm 1 DFF-Guided Calibration Training

Require: Real images $\{x_r\}$, segmentation maps $\{s\}$, frozen SUT F , ControlNet G_Θ

Require: Hyperparameters: steps $T=22000$, $\beta = 0.3$, $\lambda_{\text{dff}} = 0.08$, CF steps $K_{\text{cf}}=80$

```
1: for  $t = 1$  to  $T$  do
2:   Sample  $(x_r, s)$  from training set
3:    $x_s \leftarrow G_\Theta(s, \text{noise})$  {Generate synthetic image.}
4:    $\mathcal{L}_{\text{recon}} \leftarrow \text{MSE}(\text{predicted\_noise}, \text{target\_noise})$ 
5:    $\mathcal{L}_{\text{OV}} \leftarrow \text{MSE}(F(x_r), F(x_s))$ 
6:   if  $t \bmod 3 = 0$  then
7:      $H(F(x_r)) \leftarrow \text{CF-XAI}(F, x_r, K_{\text{cf}})$  {Decisive map via Eq. 4}
8:      $H(F(x_s)) \leftarrow \text{CF-Optimize}(F, x_s, K_{\text{cf}})$  {Decisive map for synthetic}
9:      $\mathcal{L}_{\text{DFF}} \leftarrow \text{MSE}(\text{pool}(H(F(x_r))), \text{pool}(H(F(x_s))))$ 
10:  end if
11:   $\mathcal{L}_{\text{total}} \leftarrow \mathcal{L}_{\text{recon}} + \beta \cdot \mathcal{L}_{\text{OV}} + \lambda_{\text{dff}} \cdot \mathcal{L}_{\text{DFF}}$ 
12:  Update  $\Theta$  via backpropagation on  $\mathcal{L}_{\text{total}}$ 
13: end for
14: return Calibrated generator  $G_\Theta$ 
```

Algorithm. We optimize C_η to minimize the combined loss in Eq. (5) using SGD/ES on the generator knobs; gradients do not pass through F . Decisive maps $H(F(x_r))$ and $H(F(x_s))$ are computed independently for each image in the pair using CF-XAI, then compared via D on pooled representations. Matched pairs or nearest neighbors are used, decisive sets are averaged across counterfactual (CF) seeds, and batching (i.e., computing explanations for N images in parallel) amortizes the computational cost of the CF evaluations.

V. EXPERIMENTS

We evaluate DFF on matched KITTI–VirtualKITTI2 pairs using the three SUTs and address the following two experimental objectives.

O1 (Assessment): Does DFF reveal mechanism shifts (high DFF distance) in synthetic samples that otherwise pass standard IV and OV fidelity checks?

O2 (Calibration): Does minimizing the DFF objective successfully align decisive features while maintaining non-inferior task performance (OV)?

A. Experimental Setup

Data and pairing. We evaluate on 2,126 matched KITTI–VirtualKITTI2 pairs across the five VKITTI2 scenes (Scene01, 02, 06, 18, 20), split 80/20 by scene into 1,701 calibration and 425 held-out items.

VirtualKITTI2 provides synthetic “clone” sequences that follow the same camera trajectory as the corresponding KITTI raw sequences. We form KITTI–VKITTI2 pairs by matching the scene ID, rendering variant (VirtualKITTI2’s “clone” condition replicates KITTI lighting and weather), camera (Camera_0), and frame index.

TABLE II

CALIBRATED DFF THRESHOLDS (ϵ) DEFINED AS THE 90TH AND 95TH PERCENTILES OF DFF DISTANCES ON THE **CALIBRATION SPLIT**. INTERPRETATION: ϵ_{90} IS THE THRESHOLD BELOW WHICH 90% OF CALIBRATION-SET PAIRS FALL; A HELD-OUT SYNTHETIC IMAGE PASSES IF ITS DFF DISTANCE IS BELOW ϵ .

SUT	ϵ_{90}	ϵ_{95}
Steering	0.064	0.087
YOLOP-DA	0.570	0.699
YOLOP-LL	0.582	0.736

SUTs. We use three fixed SUT heads: (i) a PilotNet-style steering angle prediction CNN; (ii) YOLOP drivable-area; (iii) YOLOP lane-line. Feature layers are conv5 (steering) and neck pre-decoder (YOLOP), selected for semantic relevance. All SUT weights are frozen (i.e., the SUTs are not trained or fine-tuned; we evaluate their fixed, pre-trained behavior).

Metrics. Details are given in Section V-B.

Calibration. We optimize generator knobs with a combined loss on IV, OV, and DFF, treating the SUT as fixed.

Full details. Optimizers, CF-XAI hyperparameters, and per-layer shapes are documented in the anonymous repository (*link hidden for review*).

Fidelity thresholds were selected based on domain standards and empirical distributions: ϵ_{out} corresponds to a high-fidelity cutoff of 0.7 similarity (e.g., $\text{IoU} \geq 0.7$), while ϵ_{dff} is set to 0.3 based on the observed loss distribution of the explainer. Appendix A summarizes the notation used in the paper.

B. Metrics and thresholds

IV (Input fidelity).: Recall from Eq. (1) that IV fidelity is defined by a distance metric D_{in} . We instantiate D_{in} using LPIPS [22] (lower is better). To facilitate visual comparison in plots where “higher is better,” we define a normalized *IV Score* as $1 - \text{LPIPS}_{\text{norm}} \in [0, 1]$, where LPIPS is clamped to $[0, 1]$. This score is used solely for visualization; the rigorous fidelity check uses the raw LPIPS distance against ϵ_{in} .

OV (Output fidelity / task loss).: For steering we use an exponential similarity score $\exp(-5 \cdot |\theta_r - \theta_s|) \in [0, 1]$, where θ denotes the predicted angle in radians and the scaling factor 5 normalizes typical angular errors to the $[0, 1]$ range (higher is better). For YOLOP heads we use IoU between predicted masks (higher is better). We refer to these collectively as OV fidelity; improvements correspond to *increases* in these scores.

DFF (Decisive-feature distance).: We compute decisive maps using a mask-and-infill counterfactual explainer applied independently to each image (real and synthetic), then compare the resulting **pooled decisive maps** by MSE (lower is better). For each SUT, we choose calibration thresholds ϵ_{90} and ϵ_{95} as the 90th and 95th percentiles of the DFF distances on the calibration split; these fixed cut-offs are then used for pass/fail decisions on the held-out split and are summarized in Table II. Full backbone choices, normalization, non-inferiority (NI) margins, and inference details are documented in the anonymous repository (*link hidden for review*).

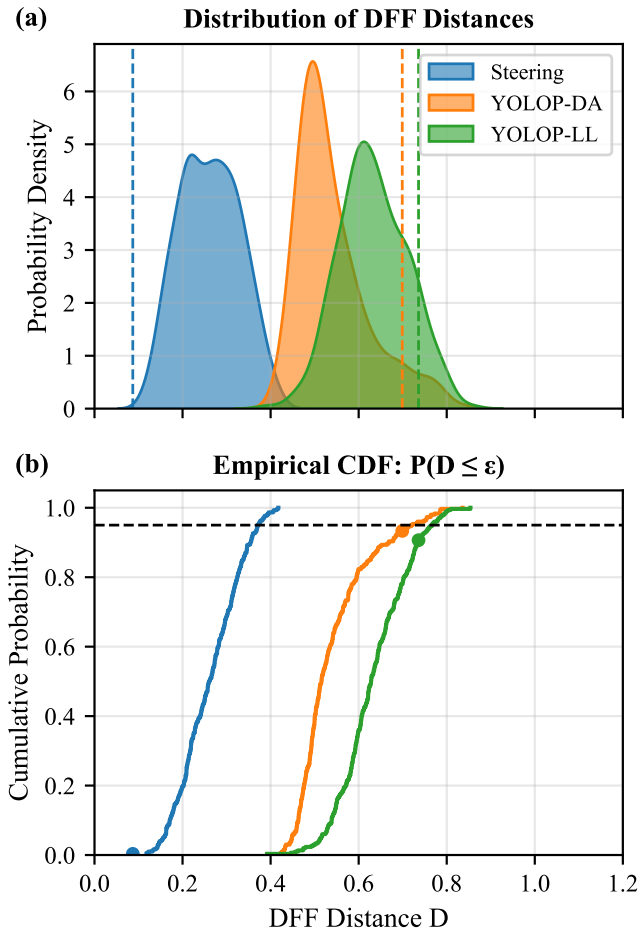


Fig. 2. Decisive-Feature Fidelity across SUTs on the same dataset. (a) Distribution of DFF distances D for Steering, YOLOP-DA, and YOLOP-LL; vertical dashed lines mark each SUT’s ε_{95} threshold. (b) Empirical CDFs $P(D \leq \varepsilon)$; the horizontal dashed line indicates 95% coverage, and markers show where each CDF crosses this level. The three curves differ substantially, confirming that DFF is SUT-specific: heads processing the same frames exhibit different decisive-feature mismatch profiles. **While OV losses are minimal (see Table III), DFF retains substantial spread**, indicating mechanism differences not captured by IV/OV.

C. Results and Analysis

At fixed thresholds determined on the calibration split (Table II), the held-out DFF distributions differ significantly by SUT (Fig. 2). In contrast, OV metrics show weak correlation with these mechanism shifts, as quantified by the low Spearman correlations in Table IV.

O1: Assessment: Table III illustrates that OV can improve without aligning decisive features, supporting the need for DFF. In the table, *Baseline* denotes uncalibrated VirtualKITT2, *OVF-X* denotes calibration optimizing only OV loss for SUT X , and *DFF-X* denotes calibration using the full objective in Eq. (5).

For **Steer**, optimizing only OV loss (*OVF-Steer*) improves LPIPS (0.610 \rightarrow 0.473) and DFF (0.361 \rightarrow 0.278), but dramatically worsens OV loss (0.0006 \rightarrow 0.3908). This occurs because the OVF optimization can overfit to perceptual similar-

TABLE III
PILOT TEST ON ONE MATCHED PAIR (SCENE20, FRAME 750). LOWER IS BETTER FOR LPIPS AND DFF. FOR OV, WE REPORT RAW TASK LOSS: MSE FOR STEERING AND $(1 - \text{IoU})$ FOR YOLOP HEADS; LOWER LOSS INDICATES BETTER OUTPUT AGREEMENT. OVF-STEER’S HIGH OV LOSS REFLECTS OVERFITTING TO PERCEPTUAL SIMILARITY AT THE EXPENSE OF TASK OUTPUT. NOTE: TABLE V REPORTS OV AS SIMILARITY SCORES (HIGHER IS BETTER) USING $\exp(-5 \cdot \text{LOSS})$ FOR STEERING AND IOU FOR YOLOP, ENABLING CLEARER INTERPRETATION OF ΔOV AS IMPROVEMENT.

SUT	Variant	LPIPS	OV loss [†]	DFF
Steer	Baseline	0.610	0.0006	0.361
	OVF-Steer	0.473	0.3908	0.278
	DFF-Steer	0.385	0.0028	0.229
DA	Baseline	0.610	0.0172	0.541
	OVF-DA	0.477	0.0044	0.630
	DFF-DA	0.390	0.0044	0.577
LL	Baseline	0.610	0.0019	0.712
	OVF-LL	0.421	0.0011	0.630
	DFF-LL	0.451	0.0013	0.635

ity at the expense of task-relevant output alignment. The *DFF-Steer* variant achieves the best DFF (0.229) while preserving OV loss near baseline levels (0.0028), demonstrating that DFF-guided calibration successfully aligns decisive features without sacrificing output fidelity.

For **DA**, OVF improves OV loss (0.0172 \rightarrow 0.0044) but worsens DFF (0.541 \rightarrow 0.630), illustrating the core problem: output-value parity without mechanism parity. The SUT produces similar outputs but relies on different decisive features. In contrast, *DFF-DA* achieves improved OV loss (0.0172 \rightarrow 0.0044) with a smaller DFF increase than OVF-DA (0.541 \rightarrow 0.577 vs. 0.541 \rightarrow 0.630), showing that aligning decisive features can mitigate mechanism divergence while benefiting output fidelity.

For **LL**, both calibration variants improve over baseline. OVF-LL achieves the best OV loss (0.0019 \rightarrow 0.0011) and also improves DFF (0.712 \rightarrow 0.630). The *DFF-LL* variant achieves competitive DFF (0.635) with similar OV loss (0.0013). For this SUT, OVF-only calibration yields slightly better DFF than the DFF-guided variant; this pattern persists in the aggregate (Table V), though both variants improve over baseline. This may reflect that for lane-line detection, optimizing output agreement incidentally aligns the decisive features the SUT uses.

These patterns support O1: OV loss can improve while DFF worsens (DA, OVF variant), demonstrating output-value parity without mechanism parity. DFF-guided calibration achieves the lowest DFF for Steering and DA while maintaining competitive OV loss; for LL, OVF-only calibration happens to yield marginally better DFF, though both variants improve substantially over baseline. The DA case most clearly illustrates the failure mode DFF is designed to reveal: OVF-DA reduces OV loss by 74% yet increases DFF by 16%, meaning the SUT produces more similar outputs but relies on more divergent decisive features.

TABLE IV
WEAK COUPLING BETWEEN OV AND DFF ON THE HELD-OUT SPLIT
(UNCALIBRATED BASELINE VARIANT). SPEARMAN ρ WITH 95% CI. LOWER $|\rho|$
SUPPORTS O1.

SUT	$\rho(\text{IV}, \text{OV})$	$\rho(\text{OV}, \text{DFF})$	95% CI
Steer	-0.022	-0.208	[-0.40, -0.01]
DA	0.211	-0.088	[-0.28, 0.11]
LL	-0.103	0.133	[-0.08, 0.33]

TABLE V
O2 CORE EFFECTS ON THE HELD-OUT SPLIT. DELTAS ARE COMPUTED AS
(DFF-CALIBRATED - UNCALIBRATED BASELINE). FOR OV (SIMILARITY,
HIGHER IS BETTER): POSITIVE ΔOV MEANS IMPROVEMENT. FOR DFF (DISTANCE,
LOWER IS BETTER): NEGATIVE ΔDFF MEANS IMPROVEMENT. ALL CHANGES
SATISFY PRE-DECLARED NON-INFERIORITY MARGINS.

SUT	ΔIV	ΔOV	ΔDFF
Steer	0.208	0.178	-0.064
DA	0.187	0.208	-0.025
LL	0.165	0.319	-0.008

The held-out distribution and CDF of DFF distances show clear SUT-specific variation while OV remains tightly clustered (Fig. 2; lower is better for DFF). The weak coupling is quantified by Spearman correlations in Table IV, confirming DFF carries information not captured by IV/OV.

Output similarity does not imply mechanism parity: DFF can remain high even when IV and OV distances are low, revealing mechanism shifts that traditional metrics miss.

Figure 3 summarizes the contrast between optimizing only for outputs and optimizing for decisive features. The OVF variants (rows 3–5) reproduce the SUT outputs on the matched scene, yet their visual evidence differs in ways that can shift the SUT’s internal reasoning. The DFF-calibrated variants (rows 6–8) keep outputs comparable while making the cues that drive the decision, such as road boundaries, lane markings, and vehicle contours, more consistent with the real frame. This aligns with our O1 claim that output similarity does not guarantee mechanism parity, and it motivates using DFF alongside IV and OV in assessment.

O2: Calibration: Table V summarizes the core effect sizes on the held-out split: DFF-guided calibration reduces DFF (negative ΔDFF , lower is better) while leaving OV loss non-inferior and slightly improved on average (positive ΔOV). Non-inferiority holds under the pre-declared margins (steering $\delta = -0.005$, YOLOP $\delta = -0.010$), corresponding to roughly 0.5% and 1% relative degradation in OV score. These thresholds were chosen a priori from pilot experiments: we identified the smallest OV drop that visibly affected downstream behavior (e.g., lane-keeping wobble), then set δ conservatively below that level.

One-sided 95% CIs for ΔOV satisfy the pre-declared margins (steering $\delta = -0.005$, YOLOP heads $\delta = -0.010$); all variants pass NI with ΔOV exceeding these thresholds (i.e., $\Delta\text{OV} > \delta$). DFF-calibrated variants do not degrade IV or OV loss and achieve negative ΔDFF on the held-out split, indicating improved decisive-feature alignment without

sacrificing task performance. The effect sizes are substantial for ΔIV and ΔOV , reflecting meaningful improvements from DFF-guided calibration. The ΔDFF values, while numerically smaller in absolute terms, represent consistent mechanism-alignment gains across all SUTs.

VI. THREATS TO VALIDITY

Our notion of mechanism parity depends on the explanation method, and we currently use a counterfactual-style explainer. All results are on camera-based KITTI and VirtualKITTI2 pairs; multi-sensor and closed-loop settings are left for future work.

Qualitative example selection. The frame shown in Fig. 3 contains faint or partially occluded lane markings, which may seem suboptimal for evaluating YOLOP-LL. We deliberately retained this frame because (i) it is representative of the dataset’s natural difficulty distribution, and (ii) it illustrates that DFF calibration improves decisive-feature alignment even when ground-truth lane cues are weak—a practically relevant regime where spurious evidence is most likely to mislead the SUT.

Decisive-set identification. We use a mask-and-infill CF-XAI estimator where each image (real or synthetic) serves as its own reference for counterfactual perturbation. The optimizer enforces sparsity and plausibility constraints, and we average over multiple CF random seeds to reduce variance. We compute D on 16×16 pooled decisive maps. We include stability checks (e.g., model-randomization sanity tests) to guard against explanation artifacts.

VII. CONCLUSION

This paper tackled a subtle but critical flaw in virtual testing: an AV system can behave the same in both real and simulated environments while using the wrong internal logic. We introduced *Decisive-Feature Fidelity (DFF)*, a new metric that measures *mechanistic realism* by checking if a given SUT relies on the same decisive features in simulation as it does in reality. Our experiments on 2126 evaluated pairs demonstrate that DFF is not just a theoretical concept. It is a practical tool that successfully identifies fidelity gaps that traditional metrics (IV and OV) cannot. On a held-out split, a DFF-guided calibration objective substantially improved DFF (reductions of 0.008–0.064 in MSE distance) while keeping OV within pre-declared non-inferiority margins and simultaneously improving IV, so DFF can be added to IV/OV checks without harming task performance.

We recommend using DFF alongside IV and OV both for *assessment* (to detect mechanism gaps that IV/OV miss) and, where feasible, for *calibration* (to close those gaps via the proposed optimization objective).

Our approach is not without limitations. (i) DFF’s validity depends on the reliability of the underlying XAI explainer; we mitigate variance with multi-seed averaging and plausibility constraints, but some noise will remain. (ii) The KITTI-VKITTI2 pairing relies entirely on the official clone scenes and frame indices in the dataset naming; while this

Figure 3: Qualitative Comparison of Calibration Methods



Fig. 3. Qualitative comparison of calibration methods on a representative KITTI–VirtualKITTI2 pair. (a) Real KITTI input. (b) Uncalibrated baseline synthetic. (c)–(e) OVF-calibrated outputs for Steering, Drivable Area, and Lane Lines respectively. (f)–(h) DFF-calibrated outputs for the same three SUTs. Each synthetic panel displays its IV score (labeled “IV”, computed as $1 - \text{LPIPS}$), OV score, and DFF distance (labeled “D”). Cyan boxes (Region A) highlight road-surface texture; magenta boxes (Region B) highlight sky and horizon. DFF calibration produces more realistic road texture and atmospheric rendering in the decisive regions, whereas OVF calibration optimises output similarity without necessarily improving perceptual realism in SUT-critical areas.

Figure 3 (Detail): Zoomed Comparison of Key Regions



Fig. 4. Zoomed comparison of decisive regions from Fig. 3. **Region A (Road):** Baseline shows unrealistic flat-green rendering; DFF-calibrated variants recover asphalt texture and lane markings. **Region B (Sky):** Baseline sky lacks atmospheric variation; DFF calibration restores realistic sky gradients and foliage detail.

gives deterministic one-to-one matches, any hidden deviations between the real and synthetic trajectories would inflate the measured DFF and thus make our reported gaps conservative. (iii) The XAI optimization is compute-heavy, though batching and partial re-use can amortize this cost.

Future work should focus on stronger estimators, broader

autonomous driving tasks (e.g., object detection, trajectory planning) and datasets, and formal theoretical analysis particularly (i) conditions under which high DFF implies high OV/SA fidelity, and (ii) sample-complexity bounds for DFF estimation. Extensions to sequence-level settings and distributional analysis over entire scenario populations are also promising directions.

Closing remark. Beyond visual realism, we believe *mechanistic realism* should be the key ingredient for trustworthy virtual testing.

ACKNOWLEDGMENTS

The authors would like to thank Siemens Industry Software Netherlands BV, a company under the laws of the Netherlands (VAT number NL 8587.14.498.B.01) whose registered office is at BIC-1, 5657 BX Eindhoven, the Netherlands, for support.

APPENDIX A
NOMENCLATURE

a_k	k -th semantic attribute in the scenario description.
v_k	Value of attribute a_k .
K	Number of attribute–value pairs in SD .
d_0	Dimensionality of the input space.
SD	Scenario description: $SD = \{(a_k, v_k)\}_{k=1}^K$.
$x \in \mathbb{R}^{d_0}$	Input datum (e.g., an image) in \mathbb{R}^{d_0} .
x_r	Real sample paired with x_s for the same scenario description.
G	Synthetic-data generator / simulator.
Θ	Configurable parameters for G .
x_s	Synthetic sample drawn as $x_s \sim G_{\Theta}(SD)$.
$RW(SD)$	Oracle set of real samples compatible with SD .
X^{cr}	Collected real-world dataset.
$\widehat{RW}(SD)$	Empirical approximation of $RW(SD)$ from X^{cr} .
F	System under test (SUT), $F : \mathbb{R}^{d_0} \rightarrow \mathbb{R}^{d_L}$.
d_L	Output dimensionality of F .
H	Explainable-AI method (e.g., CF–XAI).
$e = H(F(x))$	Explanation (e.g., heatmap) for input x .
$\mathbb{I}(\cdot)$	Indicator: 1 if its argument is true, else 0.
C_{η}	Calibrator (policy network) with parameters η .
$\Theta^* = C_{\eta}(x_s^{(init)}, SD)$	Calibrated generator parameters for scenario description SD .
ζ_k	Random seed for the k -th counterfactual mask generation.
K_{cf}	Number of CF seeds used for decisive-map averaging (Eq. 4); default value is 80 (see Algorithm 1).
ℓ	Layer index used in $F^{(\ell)}(\cdot)$.
\mathcal{L}_{recon}	Reconstruction loss for the generator.
\mathcal{L}_{OV}	Output-agreement loss (task-specific).
\mathcal{L}_{DFF}	Decisive-feature alignment loss.
β	Weight for \mathcal{L}_{OV} in calibration.
λ_{diff}	Weight for \mathcal{L}_{DFF} in calibration.

APPENDIX B
REPRODUCIBILITY NOTES

All code, configs, pairing lists, feature dumps, and trained artifacts are hosted in an anonymized repository (*(link hidden for review)*). Detailed instructions (including exact scripts, paths, and command lines) are provided in `help.md` within the repo. The repository enables reproduction of this work from cached features and includes weights/knobs for the calibrated variants (for anonymous review).

REFERENCES

- [1] ISO 34502, “Road vehicles - test scenarios for automated driving systems - scenario based safety evaluation framework,” 2022.
- [2] BSI Flex 1889, “Formalised natural language description of scenarios for automated driving systems. Specification,” 2023.
- [3] A. Dosovitskiy, G. Ros, F. Codevilla, A. Lopez, and V. Koltun, “CARLA: An Open Urban Driving Simulator,” Nov. 2017.
- [4] A. Rombach, D. Lorenz, P. Esser, and B. Ommer, “High-resolution image synthesis with latent diffusion models,” in *CVPR*, 2022. [Online]. Available: <https://arxiv.org/abs/2112.10752>

- [5] L. Zhang and M. Agrawala, “Adding conditional control to text-to-image diffusion models,” *arXiv preprint*, 2023. [Online]. Available: <https://arxiv.org/abs/2302.05543>
- [6] C.-H. Cheng, P. Stöckel, and X. Zhao, “Instance-Level Safety-Aware Fidelity of Synthetic Data and Its Calibration,” in *2024 IEEE 27th International Conference on Intelligent Transportation Systems (ITSC)*, Sep. 2024, pp. 2354–2361.
- [7] A. Stocco, B. Pulfer, and P. Tonella, “Mind the Gap! A Study on the Transferability of Virtual vs Physical-world Testing of Autonomous Driving Systems,” *IEEE Transactions on Software Engineering*, vol. 49, no. 4, pp. 1928–1940, Apr. 2023.
- [8] C. Johnson, E. Graupe, and M. Kassel, “A Literature Review of Simulation Fidelity for Autonomous-Vehicle Research and Development,” *SAE International Journal of Aerospace*, vol. 16, no. 3, pp. 253–261, May 2023.
- [9] X. Zhao, R. Aghazadeh-Chakherlou, C.-H. Cheng, P. Popov, and L. Strigini, “On the need for a statistical foundation in scenario-based testing of autonomous vehicles,” in *Proc. of the IEEE International Conference on Intelligent Transportation Systems (ITSC)*, 2025.
- [10] S. Riedmaier, T. Ponn, D. Ludwig, B. Schick, and F. Diermeyer, “Survey on scenario-based safety assessment of automated vehicles,” *IEEE Access*, vol. 8, pp. 87 456–87 477, 2020.
- [11] S. Riedmaier, B. Danquah, B. Schick, and F. Diermeyer, “A taxonomy for quality in simulation-based development and testing of automated driving systems,” *IEEE Access*, vol. 10, pp. 117 158–117 186, 2022.
- [12] S. Tang and et al., “A survey on automated driving system testing: Landscapes and trends,” *ACM Transactions on Software Engineering and Methodology*, 2023.
- [13] D. Omeiza, H. Webb, M. Jirotko, and L. Kunze, “Explanations in autonomous driving: A survey,” *IEEE Transactions on Intelligent Transportation Systems*, vol. 23, no. 8, pp. 10 142–10 162, 2022.
- [14] X. Hu, S. Li, T. Huang, B. Tang, R. Huai, and L. Chen, “How simulation helps autonomous driving: A survey of sim2real, digital twins, and parallel intelligence,” *IEEE Transactions on Intelligent Vehicles*, vol. 9, no. 1, pp. 593–612, 2024.
- [15] S. Sagmeister, P. Kounatidis, S. Goblirsch, and M. Lienkamp, “Analyzing the impact of simulation fidelity on the evaluation of autonomous driving motion control,” in *2024 IEEE Intelligent Vehicles Symposium (IV)*, 2024, pp. 230–237.
- [16] A. Geiger, P. Lenz, and R. Urtasun, “Are we ready for autonomous driving? the KITTI vision benchmark suite,” in *CVPR*, 2012, pp. 3354–3361.
- [17] J. Tobin and et al., “Domain randomization for transferring deep neural networks from simulation to the real world,” in *IROS’17*. IEEE, 2017, pp. 23–30.
- [18] S. R. Richter, V. Vineet, S. Roth, and V. Koltun, “Playing for data: Ground truth from computer games,” in *ECCV*, 2016, pp. 102–118.
- [19] Y. Cabon, N. Murray, and M. Humenberger, “Virtual KITTI 2,” *arXiv preprint*, 2020. [Online]. Available: <https://arxiv.org/abs/2001.10773>
- [20] A. Shrivastava, T. Pfister, O. Tuzel, J. Susskind, W. Wang, and R. Webb, “Learning from simulated and unsupervised images through adversarial training,” in *CVPR*, 2017.
- [21] J. Zhu, T. Park, P. Isola, and A. A. Efros, “Unpaired image-to-image translation using cycle-consistent adversarial networks,” in *ICCV*, 2017.
- [22] R. Zhang, P. Isola, A. A. Efros, E. Shechtman, and O. Wang, “The unreasonable effectiveness of deep features as a perceptual metric,” in *CVPR*, 2018.
- [23] F. U. Haq, D. Shin, S. Nejati, and L. Briand, “Can offline testing of deep neural networks replace their online testing?” *Empir. Software Eng.*, vol. 26, no. 5, p. 90, 2021.
- [24] F. Codevilla, A. M. Lopez, V. Koltun, and A. Dosovitskiy, “On offline evaluation of vision-based driving models,” in *Proceedings of the European conference on computer vision (ECCV)*, 2018, pp. 236–251.
- [25] C. Szegedy, W. Zaremba, I. Sutskever, J. Bruna, D. Erhan, I. Goodfellow, and R. Fergus, “Intriguing properties of neural networks,” in *ICLR*, 2014.
- [26] J. Adebayo, J. Gilmer, M. Muelly, I. Goodfellow, M. Hardt, and B. Kim, “Sanity checks for saliency maps,” in *NeurIPS*, 2018.
- [27] A. Ghorbani, A. Abid, and J. Zou, “Interpretation of neural networks is fragile,” in *Proc. of the AAAI conference on artificial intelligence*, vol. 33, no. 01, 2019, pp. 3681–3688.
- [28] W. Huang, X. Zhao, G. Jin, and X. Huang, “Safari: Versatile and efficient evaluations for robustness of interpretability,” in *Proc. of the IEEE/CVF international conference on computer vision*, 2023, pp. 1988–1998.

- [29] X. Zhao, W. Huang, X. Huang, V. Robu, and D. Flynn, "Baylime: Bayesian local interpretable model-agnostic explanations," in *Uncertainty in artificial intelligence*, 2021, pp. 887–896.
- [30] R. Fong and A. Vedaldi, "Interpretable explanations of black boxes by meaningful perturbations," in *ICCV*, 2017.